ADVANCES IN ATMOSPHERIC SCIENCES, 2025

• **Original Paper** •

Radiosonde Measurements and Polar WRF Simulations of Low-Level Wind Jets in the Amundsen Sea Embayment, West Antarctica

Sai Prabala Swetha CHITTELLA[1], Andrew ORR[*2], and Pranab DEB[*1]

[1]*Centre for Ocean, River, Atmosphere and Land Sciences (CORAL), Indian Institute of Technology, Kharagpur, India*

[2]*British Antarctic Survey, National Environmental Research Council, Cambridge, UK*

(Received 23 September 2024; revised 27 January 2025; accepted 6 March 2025)

ABSTRACT

We show that low-level jets (LLJs) occurred in 11 out of 22 radiosonde profiles in late austral summer over the coastal region of the Amundsen Sea Embayment, with ten of the LLJs directed offshore. The LLJs had core speeds from 9 to 32 m s^{-1}, jet core heights from 80 to 800 m, and were associated with strong, low-level temperature inversions. Seven of the observed offshore LLJs were reasonably simulated by the polar-optimized Weather Research and Forecasting (Polar WRF) model, with output from the model subsequently used to elucidate their generation mechanisms. This study shows that one of the offshore LLJs simulated by the Polar WRF was caused by katabatic winds, while the remaining six were caused by the enhancement of katabatic winds by synoptic forcing in response to a low-pressure system over the Bellingshausen Sea, i.e., the offshore wind component associated with this system plays a crucial role in the enhancement of the katabatic LLJ. Examination of the Polar WRF output further shows that the LLJs extended over large areas of the Amundsen Sea Embayment, resulting in substantially enhanced near-surface wind speeds over both the Thwaites and Pine Island ice shelves, as well as the open ocean over the continental shelf. The wind-driven forcing associated with the LLJs could perhaps have important impacts on the redistribution of snow over the ice shelves significantly, as well as to affecting sea-ice and ocean circulation variability, including the transport of relatively warm water over the continental shelf to the ice shelf cavities and extension basal melting.

Key words: low-level jets, temperature inversion, katabatic winds, synoptic forcing, Amundsen Sea Embayment, Pine Island Glacier, Thwaites Glacier

Citation: Chittella, S. P. S., A. Orr, and P. Deb, 2025: Radiosonde measurements and Polar WRF simulations of low-level wind jets in the Amundsen Sea Embayment, West Antarctica. *Adv. Atmos. Sci.*, https://doi.org/10.1007/s00376-025-4398-5.

Article Highlights:

- Low-level wind jets (LLJs) occur in the Amundsen Sea Embayment, including over the Thwaites and Pine Island ice shelves and the open ocean.
- The LLJs are caused by katabatic winds, as well as the enhancement of katabatic winds by synoptic forcing.

1. Introduction

Low-level jets (LLJs) are a relatively common feature within the stably stratified atmospheric boundary layer of the polar regions and are defined as a maximum in the vertical profile of the horizontal wind speed (e.g., Heinemann and Rose, 1990; Andreas et al., 2000; Renfrew and Anderson, 2006; Seefeldt and Cassano, 2008; Vihma et al., 2011; Tastula et al., 2012; Ebner et al., 2014; Tuononen et al., 2015; Jones et al., 2016; Heinemann and Zentek, 2021). The strong vertical wind shear associated with LLJs can influence the turbulent structure of the boundary layer and hence the exchange of momentum, heat, and moisture between the atmosphere and the surface (e.g., Heinemann and Rose, 1990; Smedman et al., 1993; Owinoh et al., 2005; Webber et al., 2017). These LLJs can exist over relatively narrow regions that extend for many hundreds of kilometers, which can influence sea ice and ocean circulation variability (Langland et al., 1989; Webber et al., 2017; Guest et al., 2018; Wang et al., 2021), as well as the horizontal transport of heat and moisture by the atmosphere (Higgins et al., 1997; Seefeldt and Cassano, 2008). They also often occur in the presence of strong, low-level temperature inversions (e.g., Andreas et al., 2000; Renfrew and Anderson, 2006; Vihma et al., 2011; Jones et al., 2016; Heinemann and Zentek, 2021; Orr et al., 2021).

In the Antarctic, LLJs can occur due to localized katabatic winds that form over the slopes of its ice sheets and glaciers (Heinemann, 1999; Renfrew and Anderson, 2006; Ranjha et al., 2013; Heinemann and Zentek, 2021). Katabatic winds can also extend far away from the slope region, including over ice shelves and the open ocean (Bromwich et al.,

* Corresponding authors: Andrew ORR, Pranab DEB
Emails: anmcr@bas.ac.uk, pranab@coral.iitkgp.ac.in

1994; Wang et al., 2021). For example, Heinemann and Zentek (2021) showed that LLJs associated with katabatic winds can occur with frequencies as high as 70% over the Weddell Sea sector of Antarctica during winter and can last for several days and have speeds between 10–20 m s^{-1} and heights mostly below 200 m. Also, in the Antarctic, the offshore wind component associated with the southern or western flanks of synoptic-scale and mesoscale cyclones can play a crucial role in the enhancement of katabatic winds, resulting in the generation of severe strong wind events (Parish and Bromwich, 1987; Van den Broeke and Van Lipzig, 2003; Steinhoff et al., 2008; Turner et al., 2009; Orr et al., 2014; Chenoli et al., 2015).

The Amundsen Sea Embayment sector of West Antarctica is recognized as an important area for katabatic wind convergence (e.g., Parish and Bromwich, 1987; Yu and Zhong, 2019) and the formation of LLJs (Jones et al., 2016). This region is also important because it drains a large part of the West Antarctic Ice Sheet into the ocean. For example, despite their small size, a substantial amount of ice discharge drains into the Amundsen Sea through ice streams such as the Pine Island and Thwaites glaciers (Mouginot et al., 2014; Turner et al., 2017). In recent decades, the ice discharge from outlet glaciers such as these has accelerated due to increased thinning of the ice shelves that buttress them, resulting in rising sea levels (Mouginot et al., 2014; Reed et al., 2024). These changes in ice shelf melting are due to increased incursions of relatively warm water onto the continental shelf of the Amundsen Sea Embayment, which is forced by changes in the regional atmospheric circulation over the continental shelf edge region (Jacobs et al., 2011; Pritchard et al., 2012; Jenkins et al., 2016). However, a thorough understanding of the local wind forcing over the continental shelf region of the Amundsen Sea Embayment in response to katabatic LLJs and their enhancement by synoptic-scale forcing is currently lacking, despite the possible influence that this could have on driving local oceanic variability and the transport of relatively warm water over the continental shelf to the ice shelf cavities, and by extension basal melting (Turner et al., 2017; Webber et al., 2017).

Radiosonde-based profiles of the atmosphere have been used in many studies to identify the occurrence and properties of LLJs in polar regions (e.g., Andreas et al., 2000; Vihma et al., 2011; Jones et al., 2016). However, these measurements are limited to a relatively small area and also are often only available from occasional research campaigns. Therefore, output from regional climate model (RCM) simulations, which include comprehensive spatial and temporal coverage, are also employed to investigate LLJs, including their climatological characteristics (Seefeldt and Cassano, 2008; Tastula et al., 2012; Ebner et al., 2014; Tuononen et al., 2015; Heinemann and Zentek, 2021). Moreover, the smaller grid spacing employed by RCMs allows an improved representation of the critical dynamical and physical processes responsible for LLJs, such as the stably stratified boundary layer and the complex and steep coastal orography of Antarctica (Orr et al., 2014).

This study uses radiosonde profiles of temperature and wind from the coastal region of the Amundsen Sea Embayment that includes the Pine Island and the Thwaites glaciers to gain a better understanding of how frequent LLJs are in this region, as well as some of the properties of the jets and their associated temperature inversions. The measurements are further used to assess the representation of LLJs in an RCM simulation using the polar-optimized Weather Research and Forecasting (Polar WRF) model. Finally, results from the Polar WRF simulation are used to investigate the generation mechanisms associated with the observed LLJs, with a special focus on the enhancement of katabatic LLJs by synoptic-scale forcing. Finally, as well as being of use in understanding the local wind regime, our results are also helpful in improving the ability of weather forecasters to predict severe and hazardous wind events to ensure the safety of aircraft, which are used for scientific and logistical operations in this area.

The remainder of this paper is structured as follows. Section 2 describes the data, model and methodology. Section 3 presents the results, and section 4 provides a discussion and a conclusion.

2. Data, model, and methods

A set of 38 radiosondes were launched during the cruise over the continental shelf region of the Amundsen Sea between 1 February 2014 and 4 March 2014 by the research vessel James Clark Ross [see Fig. 1 of Jones et al. (2016)]. Typically, one radiosonde was launched each day at around 1200 UTC, with the exception of three days that included several launches (on 13, 18, and 23 February 2014). This study uses data from 22 of these radiosondes that were chosen because they were launched around the coastal regions (see Fig. 1 for locations) and thus are more likely to be influenced by katabatic winds. Full details of the radiosonde launches are included in Jones et al. (2016). Note that low concentrations of sea ice occurred during the cruise over the period of interest (Jones et al., 2016).

The RCM simulation uses version 3.5.1 of Polar WRF, which was shown by Deb et al. (2016) to realistically simulate summer near-surface meteorological conditions over the Amundsen Sea Embayment. The model's inner domain includes the Amundsen Sea Bay sector at a grid spacing of 15 km, which is nested within a larger domain that includes much of West Antarctica and the adjacent ocean at a grid spacing of 45 km. Both domains have 70 vertical levels between the surface and the model lid at 10 hPa, with nine vertical levels between the surface and a height of around 1500 m. The model employed physics options that include a boundary layer scheme, which is particularly important for representing LLJs and temperature inversions (Tastula et al., 2012). Here, we use the Mellor-Yamada-Janjic boundary scheme (Janjic, 2002), which was shown by Deb et al. (2016) resulted in a much improved diurnal representation of temperature and wind observations over the Amundsen

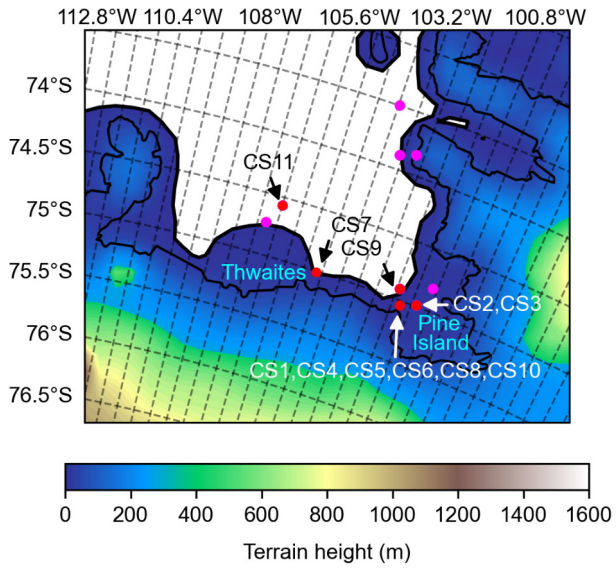

Fig. 1. Map of the coastal region of the Amundsen Sea Embayment showing the locations of the 22 radiosonde profiles examined in this study, as well as Thwaites and Pine Island glaciers and their ice shelves. The locations of the 11 radiosonde profiles that include an LLJ according to our detection criteria are shown as solid-red dots and labeled (including case studies 1 and 4 that are the focus of enhanced investigation), and the 11 that do not include an LLJ according to our detection criteria are shown as solid-magenta dots. The number of locations is less than 22, as some locations contain multiple profiles. The terrain height (shading, m), ice mask, and coastline (both continuous black lines) are taken from the Polar WRF simulation. The area in white is the continental shelf region of the Amundsen Sea.

Sea Embayment compared to either the Mellor-Yamada-Nakanishi-Niino or Yonsei University boundary layer schemes. Note that Tastula et al. (2012) showed that Polar WRF simulations with the Mellor-Yamada-Janjic scheme were relatively unsuccessful at simulating LLJs over the ice-covered Weddell Sea region of Antarctica, with only around half the number of simulated jets observed**.** The model is driven by ERA-Interim reanalysis data every 6 hours, daily satellite-based observations of sea surface temperature (Casey et al., 2010), and sea ice concentration (Comiso, 2000). The model also uses high-resolution orography from Bedmap2, as well as spectral nudging from around 1.5 km above the surface to the model top, which is a way of ensuring that the large-scale model fields in the interior domain are consistent with ERA-Interim. For further details of the model setup, please see Deb et al. (2016, 2018). The model was run from 0000 UTC 1 February 2014 to 4 March 2014. Outputs from the interior domain of the model were archived every hour.

Following Tuononen et al. (2015), a local maximum in the wind profile is classified as an LLJ if it is at least 2 m s^{-1} (absolute criteria) and 25% (relative criteria) stronger than the local minimum value above and below the maximum, and also occurs below a height of 1500 m above the surface. This definition prevents the incorrect classification of LLJs for both weak (absolute criteria) and strong (relative criteria) wind conditions. In the case that multiple local maximums in the wind profile exist below 1500 m, the LLJ is simply chosen as the maximum that is closest to the surface. The speed and height of the local maximum identified are referred to as the wind speed of the jet core and height of the jet core, respectively. The jet strength is defined as the difference between the wind speed of the jet core and the wind speed minimum above the jet (Vihma et al., 2011).

Additionally, we use the definition of Andreas et al. (2000) to identify temperature inversions. This involves scanning the temperature profile from bottom to top, with the height of the inversion base identified as the level where the sign of the vertical gradient of temperature changes from negative to positive (i.e., a local minimum). As we continue to scan upwards, the height of the inversion top is identified as the level where the temperature gradient switches again (i.e., a local maximum). Thin temperature inversions (50 m or less in thickness) that were contained within a deeper inversion were ignored. The temperature inversion strength is defined as the difference between the temperature at the inversion top and the inversion base.

3. Results

3.1. *Properties of LLJs*

Using our detection criteria, LLJs were identified in 11 out of the 22 radiosonde profiles examined (see Fig. 1 for locations). Table 1 shows the dates and times of these 11 profiles, which include three profiles on 13 February and three on 18 February. The 11 profiles are labeled Case Study 1 (CS1), Case Study 2 (CS2), …, Case Study 11 (CS11). Figure 2 displays the radiosonde wind speed profiles for each of the 11 cases showing LLJs, showing core speeds between 9 to 32 m s^{-1} and core heights from around 80 to 800 m. Also shown in Fig. 2 are the corresponding radiosonde temperature profiles, indicating the occurrence of temperature inversions for all 11 cases, with inversion base heights from around 80 to 800 m. Additionally, ten of the LLJs were directed offshore, with only the CS11 jet onshore.

Figure 3 shows how some of the properties of the observed LLJs and temperature inversions are related. This demonstrates that the speed of the jet core broadly increases with core height, although this relationship is less robust for core wind speeds below around 15 m s^{-1} (Fig. 3a). The results also show that the height of the jet core was either around or slightly lower than the inversion base, suggesting that the jets are typically embedded in the inversion layer (Fig. 3b). The exception to this relationship is CS11, which has a jet core height of 486 m and an inversion height base of 237 m and inversion height top of around 300 m, suggesting that this jet was embedded above the inversion layer. Examination of the wind speed profile for CS11 shows that it actually has a relatively well-defined ‘second’ jet at a lower

Table 1. The direction, speed, and height of the LLJ core obtained from the 11 radiosonde profiles that observed a jet, as well as the time and date of the radiosonde launches. Also shown is the height of the associated temperature inversion from the measurements, as well as whether the jet formation mechanism was due to katabatic winds (Katabatic), enhanced katabatic winds due to strengthening by cyclones (Katabatic + cyclone), or inhibition of katabatic winds by cyclones (Katabatic − cyclone). The corresponding properties simulated by the Polar WRF model are shown in brackets. N/A is shown if either the LLJ or temperature inversion is not simulated by Polar WRF.

Case study	Time (UTC) and date of radiosonde launch (Polar WRF simulation)	Direction of LLJ core (offshore or onshore) from radiosondes (Polar WRF)	Speed of LLJ core (m s^{-1}) from radiosondes (Polar WRF)	Height of LLJ core (m) from radiosondes (Polar WRF)	Height of temperature inversion base (m) from radiosondes (Polar WRF)	Formation mechanism
CS1	1300 12 Feb (1300 12 Feb)	Offshore (Offshore)	14.9 (19)	181 (183)	241 (183)	Katabatic
CS2	1330 13 Feb (1300 13 Feb)	Offshore (Offshore)	23.9 (27)	534 (623)	543 (440)	Katabatic + synoptic
CS3	1620 13 Feb (1600 13 Feb)	Offshore (Offshore)	29.7 (28.4)	797 (623)	826 (623)	Katabatic + synoptic
CS4	2045 13 Feb (2100 13 Feb)	Offshore (Offshore)	32 (30)	767 (847)	810 (623)	Katabatic + synoptic
CS5	1120 15 Feb (1600 15 Feb)	Offshore (Offshore)	13.2 (13.9)	115 (183)	131 (93)	Katabatic + synoptic
CS6	2230 16 Feb (2300 16 Feb)	Offshore (Offshore)	18 (18.7)	438 (297)	616 (N/A)	Katabatic + synoptic
CS7	1130 17 Feb (1200 17 Feb)	Offshore (Offshore)	14.3 (21.6)	367 (297)	326 (27)	Katabatic + synoptic
CS8	0800 18 Feb	Offshore (No jet)	10.5 (N/A)	82 (N/A)	82 (93)	Katabatic + synoptic
CS9	1145 18 Feb	Offshore (No jet)	9.1 (N/A)	105 (N/A)	315 (93)	Katabatic + synoptic
CS10	2130 18 Feb	Offshore (No jet)	12.6 (N/A)	448 (N/A)	473 (N/A)	Katabatic + synoptic
CS11	1210 22 Feb (0900 22 Feb)	Onshore (Offshore)	9.5 (12)	486 (182)	237 (N/A)	Katabatic − synoptic

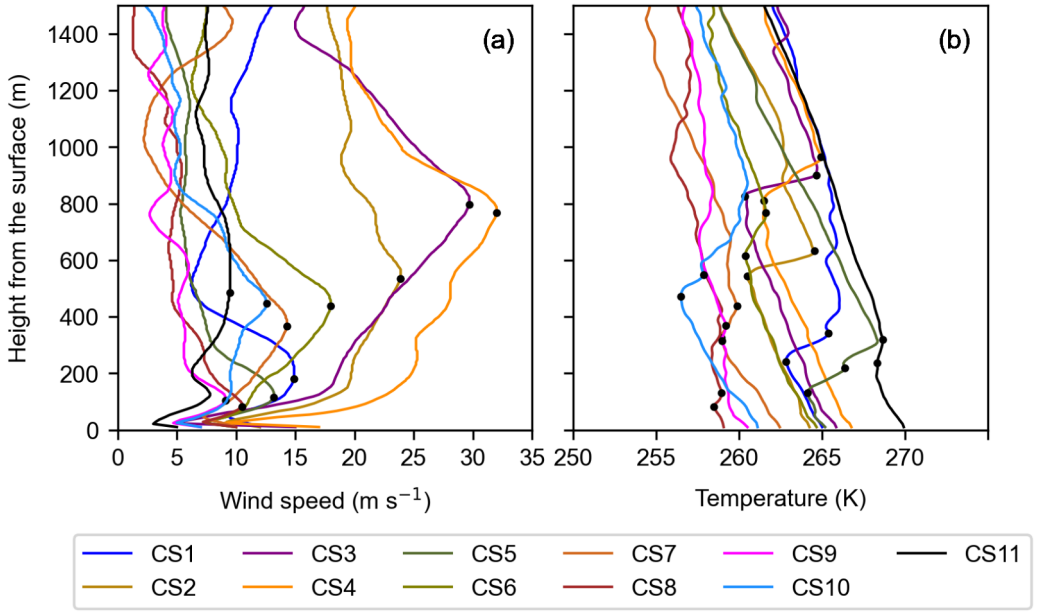

Fig. 2. Vertical profiles of (a) wind speed (m s^{-1}) and (b) temperature (K) from the 11 radiosonde profiles that observed an LLJ. Each line color refers to a particular case study. The solid-black dots show (a) the height of the LLJ core and (b) the height of the temperature inversion base and top.

height of around 150 m (Fig. 2), which is more consistent with the accompanying inversion layer. However, this jet was not selected as it failed the relative criteria test. Finally, the results also show that the jet strength broadly increases

with the inversion strength (Fig. 3c). However, two outliers failed to adhere to this relationship, CS2 and CS7, with CS2 having a much larger inversion strength relative to its jet strength compared to the other cases, whereas CS7 has a much smaller inversion strength relative to its jet strength.

3.2. *Comparison with the Polar WRF*

Table 1 compares LLJ properties between the radiosonde profiles and the Polar WRF simulation, which shows that the model simulates an LLJ for eight of the eleven cases where jets were observed, with the exceptions of CS8, CS9, and CS10. However, for two out of these eight cases (CS5 and CS11), the LLJ simulated by the Polar WRF occurred either three hours before or after the time of the observed jet. For the eight profiles where the Polar WRF simulated an LLJ, the speed of the jet core was typically higher than the measurements, with the overprediction varying from 1 m s^{-1} (CS3, CS5, CS6, CS11), to 3–4 m s^{-1} (CS1, CS2), to a maximum of 7 m s^{-1} (CS7). The only case study that underpredicted the speed of the jet core was CS4 (by −2 m s^{-1}). For the height of the jet core, the Polar WRF values were typically within around 100 m of the measured values. The exception to this was CS1, where the height of the jet core was accurately represented, and CS11, where it was underestimated by around −300 m. For CS11, the simulated height of the jet core was actually 182 m, which is more consistent with the 'second' jet at a height of around 150 m (Fig. 2), as explained above. Note that for the Polar WRF, little relationship is apparent between the size of the biases for the jet core speed and core height. For the height of the temperature inversion base, the Polar WRF values are either around the simulated height of the jet core (CS1, CS3) or around 100–200 m lower (CS2, CS4, CS5, CS7), i.e., suggesting that the jets are either embedded in the inversion layer or just below. For case studies CS6 and CS11, no temperature inversion was simulated. Finally, for the eight profiles where the Polar WRF did simulate an LLJ, it correctly represented the offshore direction of the jet in seven of these. The exception to this was CS11, where the observations showed an onshore jet and the Polar WRF an offshore jet.

To further elucidate the Polar WRF performance, Fig. 4 compares the Polar WRF and radiosonde profiles for CS1 and CS4 (see also Table 1). For CS1, the radiosonde profiles show a pronounced offshore LLJ with a core speed of 15 m s^{-1} at a height of around 181 m (Fig. 4a), which is associated with a sharp temperature inversion with a base height of 241 m and top around 300 m (Fig. 4b). The shape of the wind and temperature profiles are broadly captured by the Polar WRF, although the simulated wind speeds are around 5 m s^{-1} higher compared to the observations (from the surface to a height of 600 m), while the simulated temperatures are around 4 K lower. The simulated inversion strength is also stronger than the measured value, which is a plausible explanation as to why the simulated jet core speed is higher. For CS4, the radiosonde profiles show both a stronger and higher-altitude offshore LLJ compared to CS1. The observations show a core speed of 32 m s^{-1} at a height of around 767 m (Fig. 4c) and a sharp temperature inversion with a base height of 810 m and a top around 900 m (Fig. 4d). The wind profile and LLJ is well captured by the Polar WRF, but the temperature profile and inversion layer less so. The remainder of the results section will focus on investigating the formation mechanisms related to both of these LLJs, as well as their influence on the local-scale near-surface wind regime.

3.3. *Katabatic LLJs*

Figure 5a examines the synoptic conditions associated

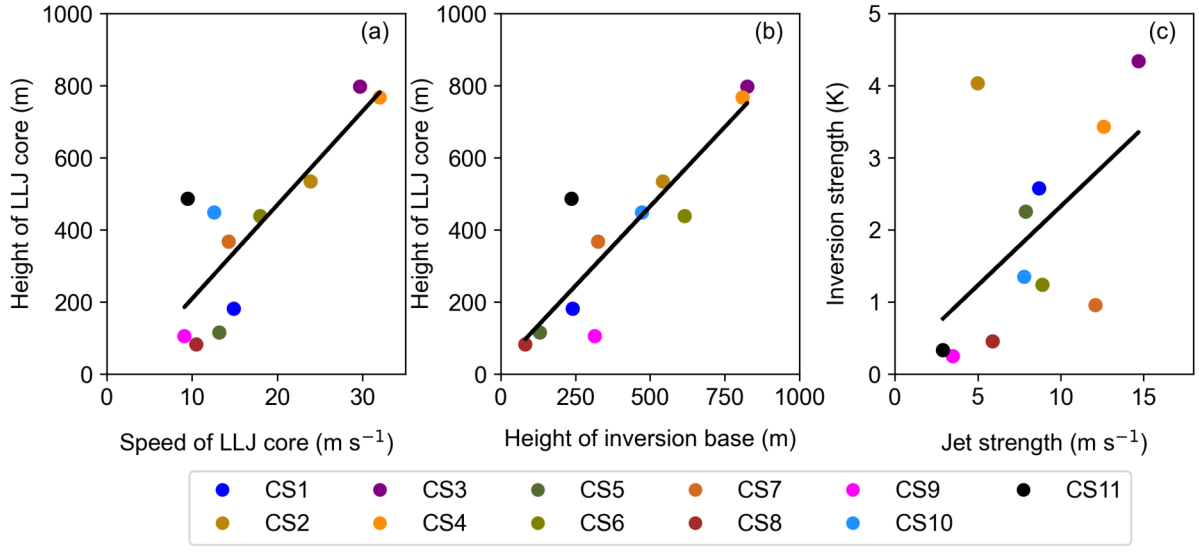

Fig. 3. Scatterplots based on measurements from the 11 radiosonde profiles that observed an LLJ in terms of the (a) speed of the LLJ core (m s^{-1}) versus height of the LLJ core (m), (b) height of the temperature inversion base (m) versus height of the LLJ core (m), and (c) LLJ jet strength (m s^{-1}) versus temperature inversion strength (K). The color of each solid dot refers to a particular case study. The linear regression estimate based on the data is shown as the black line.

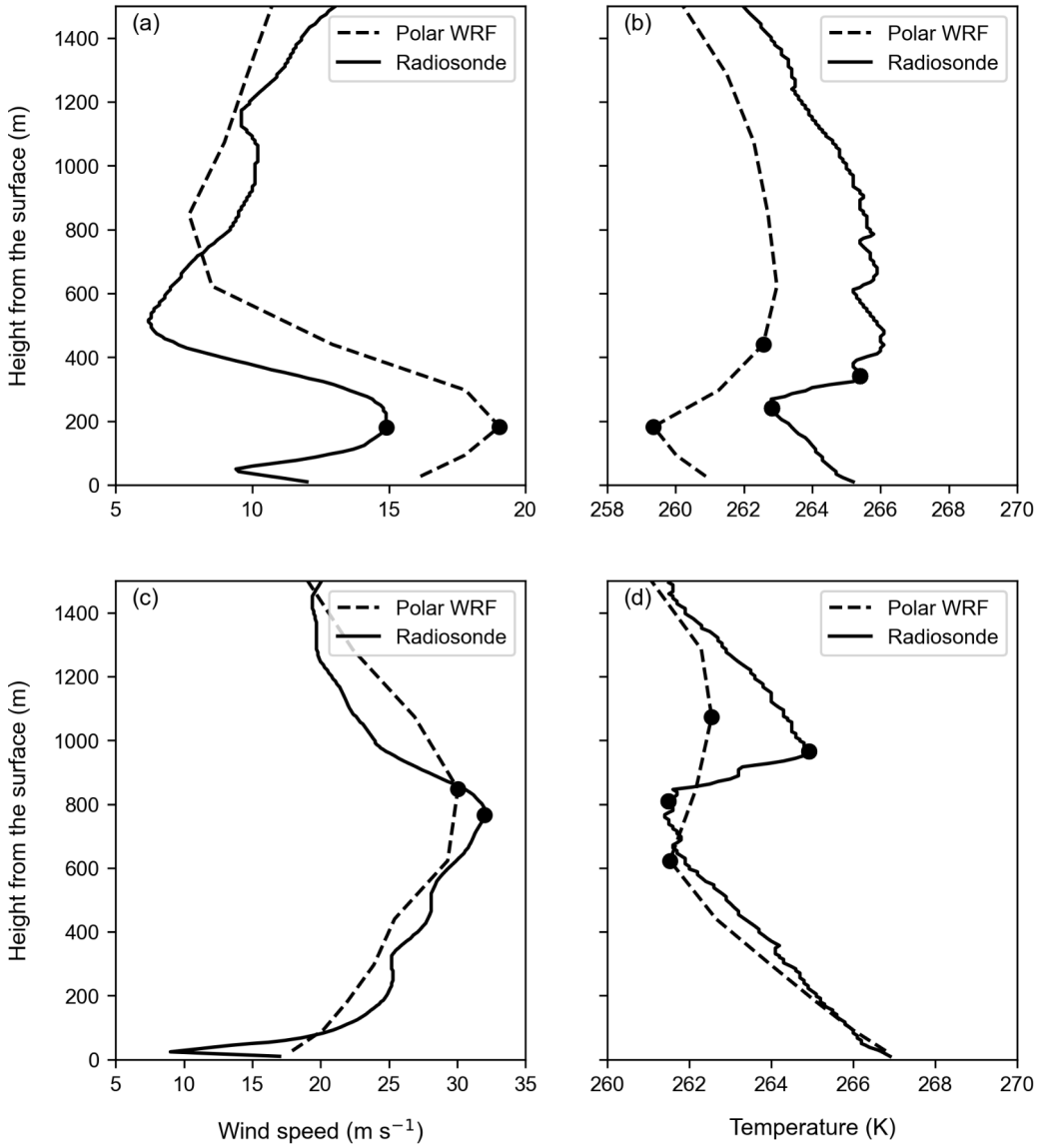

Fig. 4. Vertical profiles of wind speed (left; m s^{-1}) and temperature (right; K) based on measurements from radiosondes (solid line) and Polar WRF simulations (dashed line) for CS1 (top), CS4 (bottom). The solid-black dots shown in (a, c) indicate the height of the LLJ core and (b, d) the height of the temperature inversion base and top. The observational profiles for CS1 and CS4 are at 1300 UTC 12 Feb and at 2045 UTC 13 Feb, respectively. The model output times are at 1300 UTC 12 Feb and at 2100 UTC 13 Feb. Note the different scales for the *x*-axis.

with CS1 by showing the associated 500-hPa geopotential height and horizontal wind fields from the Polar WRF simulation. The geopotential height field shows a weak north-south dipole pattern to the east of the radiosonde launch location, with a weak low-pressure region occurring over the Bellingshausen Sea region (minimum in 500-hPa geopotential height of 5040 m), which acts to generate the band of southerlies over the eastern section of the West Antarctic ice sheet and the Amundsen Sea Embayment. An examination of the geopotential height at other pressure levels shows that this low-pressure region is apparent throughout much of the troposphere (not shown).

To examine the local-scale conditions associated with these synoptic conditions, Fig. 6a shows the Polar WRF simulated winds along a vertical cross-section that passes through the location of the CS1 radiosonde launch and aligned in the direction of the observed offshore jet (shown as the line A-B in Fig. 5a). This transect begins (upwind) over the coastal slopes, passes over the Pine Island ice shelf, and finishes (downwind) over the open ocean. Over the coastal slopes, there is an enhancement of both the along- and cross-transect wind speeds over a relatively shallow layer above the surface. In contrast, the winds at upper levels are relatively weak (<5 m s^{-1}). In the along-transect direction, the winds in the near-surface layer accelerate downslope to speeds exceeding 20 m s^{-1}, with a peak speed of around

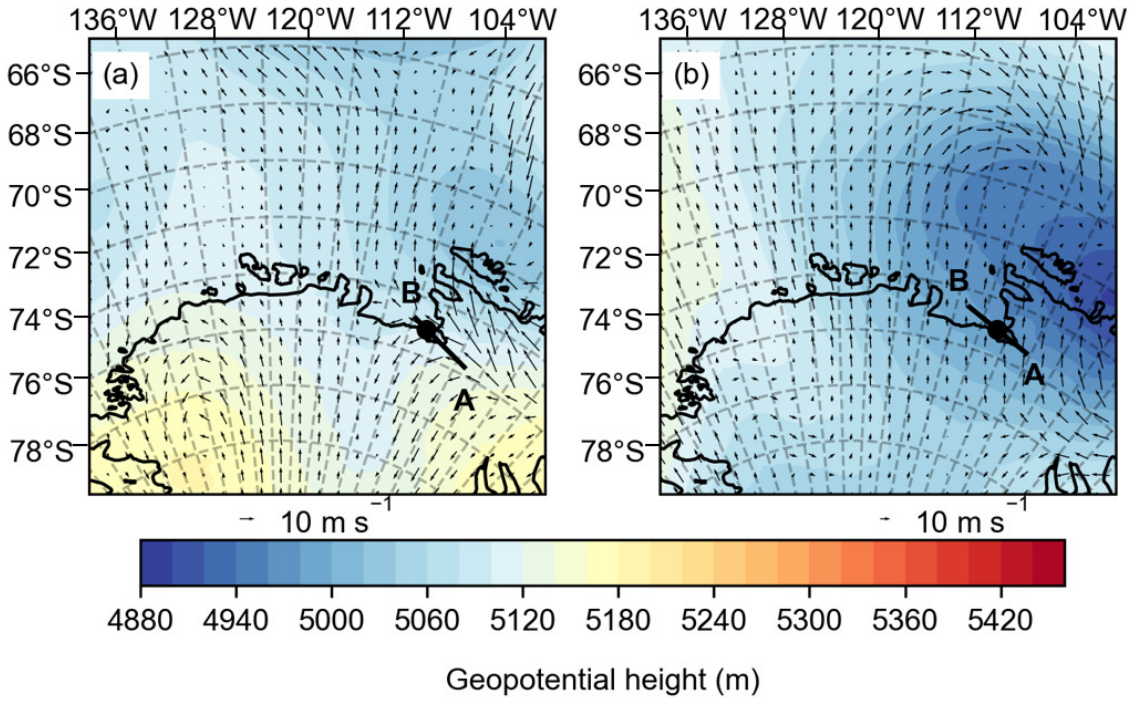

Fig. 5. Polar WRF simulation of the 500-hPa geopotential height (shading, m) and 500-hPa horizontal wind (vectors, m s^{-1}) for (a) CS1 at 1300 UTC 12 Feb and (b) CS4 at 2100 UTC 13 Feb. The solid-black dot denotes the location of the radiosonde launch for each case study. The thick line labeled A-B indicates the vertical transects that are examined in Fig. 6, which pass through the respective launch location of the radiosonde and are aligned in the direction (broadly northwest orientation) of the observed LLJ. The coastline is denoted by the continuous black line.

24 m s^{-1} occurring around 153 km along the transect, which coincides with the steepest local topography gradient. The associated cross-transect wind speeds are positive (i.e., to the right of the along-transect direction, looking downwind) and much weaker (2–4 m s^{-1}), which is likely due to the influence of the synoptic-scale forcing. Examination of the associated vertical cross-section of temperature over the downslope region shows an inversion layer at around 200 m above the surface (not shown). Therefore, these downslope winds are consistent with katabatic winds and a relatively low-level inversion layer trapping colder (and therefore heavier) air below, which acts to intensify the winds.

Due to the close proximity of the radiosonde launch location to the calving front of the Pine Island ice shelf, it is evident from Fig. 6a that the observed LLJ occurs due to the katabatic winds extending across the ice shelf and eventually over the open ocean. It is also apparent that although the katabatic winds begin to decelerate over the open ocean, they still maintain their identity over the entire transect, i.e., some distance seaward of the edge of the ice shelf. The signature of a katabatic LLJ over the ice shelf and open ocean regions of Amundsen Sea Embayment is also apparent in the 10-m wind speed field simulated by the model (Fig. 7a). This shows wind speeds reaching 18 m s^{-1} over parts of the Thwaites and Pine Island ice shelves and the ocean immediately adjacent to them. Moreover, a region of enhanced wind speeds of around 10 m s^{-1} is shown over a large part of the Amundsen Sea Embayment, with much weaker wind speeds over the eastern and western sections of the coastline. However, it is likely that Polar WRF could be overpredicting the strength and reach of these winds, as Fig. 4a showed a positive wind-speed bias for CS1.

3.4. *Enhancement of katabatic LLJs by synoptic forcing*

Figure 5b shows the synoptic conditions associated with CS4, which occurred around 32 hours after CS1 (Table 1). During this period, the low-pressure system over the Bellingshausen Sea region remained stationary and substantially deepened (minimum in 500-hPa geopotential height of 4920 m), which again acts to generate the band of southerlies situated over the Antarctic ice sheet and Amundsen Sea Embayment. Although there is comparatively little difference in strength of the southerlies at 500 hPa between CS1 and CS4, further examination shows that 850-hPa wind speed over the coastal region of the Amundsen Sea Embayment increases from around 15 m s^{-1} for CS1 to around 30 m s^{-1} CS4 (not shown), i.e., consistent with a deepening of the low-pressure system.

Figure 6b shows the Polar WRF simulated winds along a vertical cross-section that passes through the location of the CS4 radiosonde launch (shown as line A-B in Fig. 5b). Over the coastal slopes, there is a clear maximum in the along-transect winds around 700 m above the surface, with wind speeds reaching up to 36 m s^{-1}. Consequently, strong vertical wind shear above and below the region of peak winds is also apparent. The cross-transect wind speeds are rel-

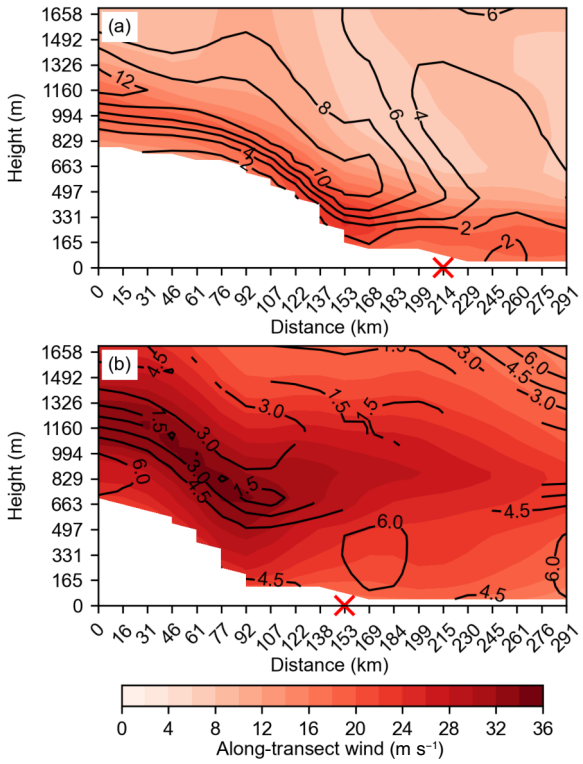

Fig. 6. Polar WRF simulation of the vertical cross-section of the along-transect wind speed (shading, m s^{-1}) and cross-transect wind speed (contours, m s^{-1}) along the A-B transect shown in Fig. 5 for (a) CS1 at 1300 UTC 12 Feb and (b) CS4 at 2100 UTC on 13 Feb. The red cross on the x-axis represents the location of the radiosonde launch in each case study, which was close to the calving front of the Pine Island ice shelf (see Fig. 1). Consequently, the region to the right of this location in each panel is mostly over the open ocean.

atively weak over the coastal slopes (<5 m s^{-1}). Examination of the associated vertical cross-section of temperature over the downslope region also shows an inversion layer around 800 m above the surface (not shown). These downslope winds are therefore consistent with a substantial strengthening of the katabatic LLJ in CS1 in response to a deepening of the low-pressure system over the Bellingshausen Sea, i.e., the offshore wind component associated with this system plays a crucial role in the enhancement of the katabatic LLJ.

Due to the close proximity of the radiosonde launch location to the calving front of the ice shelf, it is yet again evident that the observed LLJ occurs due to the enhanced katabatic wind extending across the ice shelf and eventually over the open ocean (Fig. 6b). The LLJ is subsequently shown to attenuate over a distance of 100–150 km over the open ocean. Figure 7b shows that the 10-m wind speed associated with the LLJ reaches up to 24 m s^{-1} over the coastal slopes, which is over twice as strong as the winds in this region during CS1 (Fig. 7a). These enhanced 10-m winds continue over the ice shelves and open ocean, with speeds of up to 18 m s^{-1} over much of the eastern section of the Amundsen Sea Embayment (Fig. 7b).

Finally, for the remaining five cases where the Polar WRF model correctly simulated an offshore LLJ (CS2, CS3, CS5, CS6, and CS7), examination of the associated 500-hPa geopotential height and horizontal wind fields showed that in each case, the jet was due to a substantial strengthening of the katabatic LLJ in response to a deepening of the low-pressure system over the Bellingshausen Sea [Fig. S1 of electronic supplementary file material (ESM)]. Moreover, in each of the five cases, this resulted in enhanced 10-m winds over the ice shelves and open ocean, especially over the eastern section of the Amundsen Sea Embayment (Fig. S2 in the ESM). Note that the observations showed an onshore LLJ in CS11, which was due to onshore winds associated with the eastern flank of a cyclone, which acted to dampen/inhibit the katabatic wind at the same time (not shown).

4. Discussion and conclusions

In this study, we have shown that LLJs occurred in 11 out of 22 radiosonde profiles that were launched close to the coastal region of the Amundsen Sea Embayment, including the Pine Island and Thwaites glaciers. The profiles further show that the jets were predominately offshore (in 10 out of 11 profiles), had core speeds from 9 to 32 m s^{-1}, jet core heights from around 80 to 800 m, and are accompanied by strong, low-level temperature inversions (Table 1, Fig. 2). Our results further show that: (1) the jet core heights were around or slightly lower than the inversion base, suggesting that the jets are typically embedded in the inversion layer (also shown by Andreas et al., 2000), (2) the speed of the jet core broadly increases with core height, and (3) the jet strength broadly increases with the inversion strength (Fig. 3). We further show that a simulation using the Polar WRF model at a grid spacing of 15 km is able to correctly simulate LLJs for eight of the eleven profiles, and temperature inversions for nine of the eleven profiles. However, the speed of the jet core simulated by the Polar WRF was typically higher than the measurements (positive bias of between 1 and 7 m s^{-1}), while the height of the simulated jet core was typically within around 100 m of the measurements (Table 1, Fig. 4). This level of accuracy for the height of the simulated jet core is likely reasonable given that the vertical resolution of the model was comparatively limited (and much coarser than the observations).

Output from the Polar WRF model was subsequently used to elucidate the generation mechanisms of the seven offshore LLJs that were successfully simulated. Although the Amundsen Sea Embayment sector of West Antarctica is already recognized as an important area for katabatic wind convergence (e.g., Parish and Bromwich, 1987; Yu and Zhong, 2019), this study showed that one of the offshore LLJs simulated by the Polar WRF was caused by katabatic winds, while the remaining six were caused by the enhancement of katabatic winds by synoptic forcing from a low-pressure system over the Bellingshausen Sea (Table 1, Figs. 5,

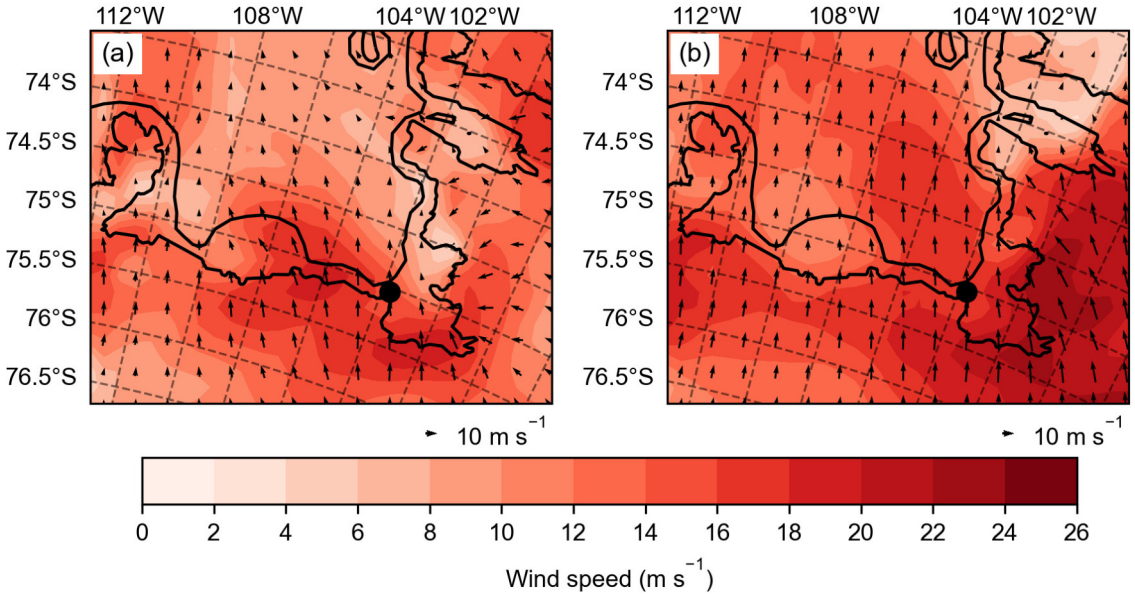

Fig. 7. Polar WRF simulation of the 10-m wind speed (shading, m s^{-1}) and vectors (arrows, m s^{-1}) for (a) CS1 at 1200 UTC 12 Feb and (b) CS4 at 2100 UTC 13 Feb. The solid-black dot denotes the location of the radiosonde launch for each case study. The domain is the same as shown in Fig. 1, with both the coastline and ice mask shown as a continuous black line.

6, S1 in the ESM).

We also examined the wind speed profiles of the other 11 radiosonde soundings that did not exhibit LLJs according to our detection criteria. Among these, five profiles still showed an offshore LLJ, but these were not identified by our criteria because they failed to meet the relative criterion, which aims to prevent the misidentification of LLJs during strong wind conditions (not shown). Analysis of the local and synoptic conditions simulated by the Polar WRF for these cases suggests that three of the five cases were caused by katabatic winds, while the remaining two cases were caused by the enhancement of katabatic winds by synoptic forcing associated with a low-pressure system. In the other six profiles, jet-like features were not observed, likely due to both weak katabatic winds and/or weak synoptic forcing.

Output from the Polar WRF simulation was further used to show that the LLJs extend over substantial areas of the Amundsen Sea Embayment, including both the Thwaites and Pine Island ice shelves and the open ocean (Figs. 6, 7, S2). These results are consistent with other studies, such as Bromwich et al. (1994) and Wang et al. (2021), which also showed that katabatic winds can extend many hundreds of kilometers out from the slope region. Over the ice shelves, the enhanced near-surface wind speeds associated with the LLJs could be responsible for the redistribution of snow over the ice shelves and enhanced snow sublimation, which could influence the surface mass balance (Mottram et al., 2021). Additionally, the redistribution of snow could also possibly affect thresholds for surface melting of the ice shelves, as this has been found to be controlled by snow accumulation (van Wessem et al., 2023). Additionally, the strong vertical wind shear/mixing associated with katabatic winds (evident in Fig. 6b) is often associated with warm signatures over ice shelves, which could facilitate melting (Heinemann et al., 2019; Orr et al., 2023). Over the open ocean, the enhanced near-surface winds speeds could potentially affect the local ocean circulation, formation of polynyas, and advection of sea-ice (Langland et al., 1989; Webber et al., 2017; Guest et al., 2018; Wang et al., 2021). Crucially, over the continental shelf of the Amundsen Sea Embayment, the local wind forcing could, therefore, influence the transport of relatively warm water over the continental shelf to the ice shelf cavities, serving to enhance basal melting (Turner et al., 2017; Webber et al., 2017).

Finally, the period examined was mainly during February 2014, i.e., late austral summer. Although our results suggest that LLJs are fairly ubiquitous in the Amundsen Sea Embayment during this period, it would be expected that they might be even more frequent during austral winter, as katabatic winds are strongest during this season (e.g., Parish and Bromwich, 1987; Yu and Zhong, 2019). However, although the density of cyclones is typically greater in Antarctica during winter, this is not the case for the Amundsen Sea and Bellingshausen Sea (Simmonds et al., 2003). This is due to the annual cycle of the longitudinal position of the Amundsen Sea Low, which shifts westward between summer and winter (Hosking et al., 2013). Therefore, it is suggested that further work should focus on producing model-based climatologies of LLJs for this region for different seasons.

Acknowledgements. The authors would like to thank Ian RENFREW and Richard W. JONES, at the University of East Anglia and Met Office, respectively, for their contributions to launching the radiosondes during the iSTAR field campaign in 2014. AO

received support from the European Union's Horizon 2020 research and innovation framework program under Grant No. 101003590 (PolarRES). SPSC and PD received funding from the Indian Institute of Technology Kharagpur and the Ministry of Education, Government of India. The authors would like to express their gratitude to the anonymous reviewers for their valuable feedback and insightful suggestions.

Electronic supplementary material: Supplementary material is available in the online version of this article at https://doi.org/10.1007/s00376-025-4398-5.

REFERENCES

Andreas, E. L., K. J. Claffy, and A. P. Makshtas, 2000: Low-level atmospheric jets and inversions over the western Weddell Sea. *Bound.-Layer Meteorol.*, **97**(3), 459–486, https://doi.org/10.1023/A:1002793831076.

Bromwich, D. H., Y. Du, and T. R. Parish, 1994: Numerical simulation of winter katabatic winds from West Antarctica crossing siple coast and the Ross Ice Shelf. *Mon. Wea. Rev.*, **122**(7), 1417–1435, https://doi.org/10.1175/1520-0493(1994)122<1417:NSOWKW>2.0.CO;2.

Casey, K. S., T. B. Brandon, P. Cornillon, and R. Evans, 2010: The past, present, and future of the AVHRR pathfinder SST program. *Oceanography from Space: Revisited*, V. Barale, J. F. R. Gower, and L. Alberotanza, Eds., Springer, 273–287, https://doi.org/10.1007/978-90-481-8681-5_16.

Chenoli, S. N., J. Turner, and A. A. Samah, 2015: A strong wind event on the Ross Ice Shelf, Antarctica: A case study of scale interactions. *Mon. Wea. Rev.*, **143**(10), 4163–4180, https://doi.org/10.1175/MWR-D-15-0002.1.

Comiso, J.J., 2000. Bootstrap sea ice concentrations from Nimbus-7 SMMR and DMSP SSM/I-SSMIS, version 2. [Available online from https://cir.nii.ac.jp/crid/1883398392268141312]

Deb, P., A. Orr, J. S. Hosking, T. Phillips, J. Turner, D. Bannister, J. O. Pope, and S. Colwell, 2016: An assessment of the Polar Weather Research and Forecasting (WRF) model representation of near-surface meteorological variables over West Antarctica. *J. Geophys. Res.: Atmos.*, **121**(4), 1532–1548, https://doi.org/10.1002/2015JD024037.

Deb, P., Orr, A., Bromwich, D. H., Nicolas, J. P., Turner, J., & Hosking, J. S., 2018: Summer drivers of atmospheric variability affecting ice shelf thinning in the Amundsen Sea Embayment, West Antarctica. *Geophysical Research Letters*, **45**(9), 4124–4133. https://doi.org/10.1029/2018GL077092.

Ebner, L., G. Heinemann, V. Haid, and R. Timmermann, 2014: Katabatic winds and polynya dynamics at Coats Land, Antarctica. *Antarctic Science*, **26**(3), 309–326, https://doi.org/10.1017/S0954102013000679.

Guest, P., P. O. G. Persson, S. P. Wang, M. Jordan, Y. Jin, B. Blomquist, and C. Fairall, 2018: Low-level baroclinic jets over the new Arctic Ocean. *J. Geophys. Res.: Oceans*, **123**(6), 4074–4091, https://doi.org/10.1002/2018JC013778.

Heinemann, G., 1999: The KABEG'97 field experiment: An aircraft-based study of Katabatic wind dynamics over the Greenland ice sheet. *Bound.-Layer Meteorol.*, **93**(1), 75–116, https://doi.org/10.1023/A:1002009530877.

Heinemann, G., and L. Rose, 1990: Surface energy balance, parameterizations of boundary-layer heights and the application of resistance laws near an Antarctic Ice Shelf front. *Bound.-Layer Meteorol.*, **51**(1–2), 123–158, https://doi.org/10.1007/BF00120464.

Heinemann, G., and R. Zentek, 2021: A model-based climatology of low-level jets in the Weddell Sea region of the Antarctic. *Atmosphere*, **12**(12), 1635, https://doi.org/10.3390/ATMOS12121635.

Heinemann, G., L. Glaw, and S. Willmes, 2019: A satellite-based climatology of wind-induced surface temperature anomalies for the Antarctic. *Remote Sensing*, **11**(13), 1539, https://doi.org/10.3390/RS11131539.

Higgins, R. W., Y. Yao, E. S. Yarosh, J. E. Janowiak, and K. C. Mo, 1997: Influence of the great plains low-level jet on summertime precipitation and moisture transport over the Central United States. *J. Climate*, **10**(3), 481–507, https://doi.org/10.1175/1520-0442(1997)010<0481:IOTGPL>2.0.CO;2.

Hosking, J. S., A. Orr, G. J. Marshall, J. Turner, and T. Phillips, 2013: The influence of the Amundsen–Bellingshausen Seas low on the climate of West Antarctica and its representation in coupled climate model simulations. *J. Climate*, **26**(17), 6633–6648, https://doi.org/10.1175/JCLI-D-12-00813.1.

Jacobs, S. S., A. Jenkins, C. F. Giulivi, and P. Dutrieux, 2011: Stronger ocean circulation and increased melting under Pine Island Glacier ice shelf. *Nature Geoscience*, **4**(8), 519–523, https://doi.org/10.1038/ngeo1188.

Janjic, Z., 2002: Nonsingular Implementation of the Mellor-Yamada Level 2.5 Scheme in the NCEP Meso model (NCEP Office Note No. 437). *NCEP, Camp Springs, Md, 555*. [Available online from https://repository.library.noaa.gov/view/noaa/11409]

Jenkins, A., P. Dutrieux, S. Jacobs, E. J. Steig, G. H. Gudmundsson, J. Smith, and K. J. Heywood, 2016: Decadal ocean forcing and Antarctic ice sheet response: Lessons from the Amundsen Sea. *Oceanography*, **29**(4), 106–117, https://doi.org/10.5670/OCEANOG.2016.103.

Jones, R. W., I. A. Renfrew, A. Orr, B. G. M. Webber, D. M. Holland, and M. A. Lazzara, 2016: Evaluation of four global reanalysis products using in situ observations in the Amundsen Sea Embayment, Antarctica. *J. Geophys. Res: Atmos.*, **121**(11), 6240–6257, https://doi.org/10.1002/2015JD024680.

Langland, R. H., P. M. Tag, and R. W. Fett, 1989: An ice breeze mechanism for boundary-layer jets. *Bound.-Layer Meteorol.*, **48**(1–2), 177–195, https://doi.org/10.1007/BF00121789.

Mottram, R., and Coauthors, 2021: What is the surface mass balance of Antarctica? An intercomparison of regional climate

model estimates. *The Cryosphere*, **15**(8), 3751–3784, https://doi.org/10.5194/TC-15-3751-2021.

Mouginot, J., E. Rignot, and B. Scheuchl, 2014: Sustained increase in ice discharge from the Amundsen Sea Embayment, West Antarctica, from 1973 to 2013. *Geophys. Res. Lett.*, **41**(5), 1576–1584, https://doi.org/10.1002/2013GL059069.

Orr, A., T. Phillips, S. Webster, A. Elvidge, M. Weeks, S. Hosking, and J. Turner, 2014: Met Office Unified Model high-resolution simulations of a strong wind event in Antarctica. *Quart. J. Roy. Meteor. Soc.*, **140**(684), 2287–2297, https://doi.org/10.1002/QJ.2296.

Orr, A., and Coauthors, 2021: Comparison of kilometre and sub-kilometre scale simulations of a foehn wind event over the Larsen C Ice Shelf, Antarctic Peninsula using the Met Office Unified Model (MetUM). *Quart. J. Roy. Meteor. Soc.*, **147**(739), 3472–3492, https://doi.org/10.1002/QJ.4138.

Orr, A., and Coauthors, 2023: Characteristics of surface "Melt Potential" over Antarctic ice shelves based on regional atmospheric model simulations of summer air temperature extremes from 1979/80 to 2018/19. *J. Climate*, **36**(10), 3357–3383, https://doi.org/10.1175/JCLI-D-22-0386.1.

Owinoh, A. Z., J. C. R. Hunt, A. Orr, P. Clark, R. Klein, H. J. S. Fernando, and F. T. M. Nieuwstadt, 2005: Effects of changing surface heat flux on atmospheric boundary-layer flow over flat terrain. *Bound.-Layer Meteorol.*, **116**(2), 331–361, https://doi.org/10.1007/S10546-004-2819-Z.

Parish, T. R., and D. H. Bromwich, 1987: The surface windfield over the Antarctic ice sheets. *Nature*, **328**(6125), 51–54, https://doi.org/10.1038/328051a0.

Pritchard, H. D., S. R. M. Ligtenberg, H. A. Fricker, D. G. Vaughan, M. R. Van Den Broeke, and L. Padman, 2012: Antarctic ice-sheet loss driven by basal melting of ice shelves. *Nature*, **484**(7395), 502–505, https://doi.org/10.1038/NATURE10968.

Ranjha, R., G. Svensson, M. Tjernström, and A. Semedo, 2013: Global distribution and seasonal variability of coastal low-level jets derived from ERA-Interim reanalysis. *Tellus A: Dynamic Meteorology and Oceanography*, **65**, 20412, https://doi.org/10.3402/TELLUSA.V65I0.20412.

Reed, B., J. A. M. Green, A. Jenkins, and G. H. Gudmundsson, 2024: Recent irreversible retreat phase of Pine Island Glacier. *Nature Climate Change*, **14**(1), 75–81, https://doi.org/10.1038/s41558-023-01887-y.

Renfrew, I. A., and P. S. Anderson, 2006: Profiles of katabatic flow in summer and winter over Coats Land, Antarctica. *Quart. J. Roy. Meteor. Soc.*, **132**(616), 779–802, https://doi.org/10.1256/QJ.05.148.

Seefeldt, M. W., and J. J. Cassano, 2008: An analysis of low-level jets in the greater Ross Ice Shelf region based on numerical simulations. *Mon. Wea. Rev.*, **136**(11), 4188–4205, https://doi.org/10.1175/2008MWR2455.1.

Simmonds, I., K. Keay, and E. P. Lim, 2003: Synoptic activity in the seas around Antarctica. *Mon. Wea. Rev.*, **131**(2), 272–288, https://doi.org/10.1175/1520-0493(2003)131<027:SAITSA>2.0.CO;2.

Smedman, A.-S., M. Tjernström, and U. Högström, 1993: Analysis of the turbulence structure of a marine low-level jet. *Bound.-Layer Meteorol.*, **66**, 105–126, https://doi.org/10.1007/BF00705462.

Steinhoff, D. F., D. H. Bromwich, M. Lambertson, S. L. Knuth, and M. A. Lazzara, 2008: A dynamical investigation of the May 2004 McMurdo Antarctica severe wind event using AMPS. *Mon. Wea. Rev.*, **136**(1), 7–26, https://doi.org/10.1175/2007MWR1999.1.

Tastula, E. M., T. Vihma, and E. L. Andreas, 2012: Evaluation of Polar WRF from modeling the atmospheric boundary layer over Antarctic Sea Ice in autumn and winter. *Mon. Wea. Rev.*, **140**(12), 3919–3935, https://doi.org/10.1175/MWR-D-12-00016.1.

Tuononen, M., V. A. Sinclair, and T. Vihma, 2015: A climatology of low-level jets in the mid-latitudes and polar regions of the Northern Hemisphere. *Atmospheric Science Letters*, **16**(4), 492–499, https://doi.org/10.1002/ASL.587

Turner, J., S. N. Chenoli, A. Abu Samah, G. Marshall, T. Phillips, and A. Orr, 2009: Strong wind events in the Antarctic. *J. Geophys. Res.: Atmos.*, **114**(D18), D18103, https://doi.org/10.1029/2008JD011642.

Turner, J., A. Orr, G. H. Gudmundsson, A. Jenkins, R. G. Bingham, C. D. Hillenbrand, and T. J. Bracegirdle, 2017: Atmosphere-ocean-ice interactions in the Amundsen Sea Embayment, West Antarctica. *Rev. Geophys.*, **55**(1), 235–276, https://doi.org/10.1002/2016RG000532.

Van den Broeke, M. R., and N. P. M. Van Lipzig, 2003: Factors controlling the near-surface wind field in Antarctica. *Mon. Wea. Rev.*, **131**(4), 733–743, https://doi.org/10.1175/1520-0493(2003)131<0733:FCTNSW>2.0.CO;2.

van Wessem, J. M., M. R. van den Broeke, B. Wouters, and S. Lhermitte, 2023: Variable temperature thresholds of melt pond formation on Antarctic ice shelves. *Nature Climate Change*, **13**(2), 161–166, https://doi.org/10.1038/s41558-022-01577-1.

Vihma, T., T. Kilpeläinen, M. Manninen, A. Sjöblom, E. Jakobson, T. Palo, J. Jaagus, and M. Maturilli, 2011: Characteristics of temperature and humidity inversions and low-level jets over Svalbard fjords in spring. *Advances in Meteorology*, **2011**(1), 486807, https://doi.org/10.1155/2011/486807.

Wang, X. Q., Z. R. Zhang, X. Z. Wang, T. Vihma, M. Zhou, L. J. Yu, P. Uotila, and D. V. Sein, 2021: Impacts of strong wind events on sea ice and water mass properties in Antarctic coastal Polynyas. *Climate Dyn.*, **57**(11–12), 3505–3528, https://doi.org/10.1007/S00382-021-05878-7.

Webber, B. G. M., and Coauthors, 2017: Mechanisms driving variability in the ocean forcing of Pine Island Glacier. *Nature Communications*, **8**(1), 14507, https://doi.org/10.1038/ncomms14507.

Yu, L. J., and S. Y. Zhong, 2019: Strong wind speed events over Antarctica and its surrounding oceans. *J. Climate*, **32**(12), 3451–3470, https://doi.org/10.1175/JCLI-D-18-0831.1.